

1  
2  
3  
4  
5  
6  
7  
8  
9  
10  
11  
12  
13  
14  
15  
16  
17  
18  
19  
20  
21  
22  
23  
24

## **Diffuse Whistler-Mode Waves Detected by Kaguya in the Lunar Polar Region**

**T. Nakagawa<sup>1</sup>, F. Takahashi<sup>2</sup>, H. Shimizu<sup>3</sup>, and Y. Saito<sup>4</sup>**

<sup>1</sup>Department of Information and Communication Engineering, Tohoku Institute of Technology, Miyagi, 982-8577 Japan.

<sup>2</sup>Department of Earth and Planetary Sciences, Faculty of Science, Kyushu University, Fukuoka 819-0395.

<sup>3</sup>Earthquake Research Institute, University of Tokyo, Tokyo 113-0032, Japan.

<sup>4</sup>Institute of Space and Astronautical Science, Japan Aerospace Exploration Agency, Kanagawa, 229-8510 Japan.

Corresponding author: Tomoko Nakagawa ([nakagawa@tohtech.ac.jp](mailto:nakagawa@tohtech.ac.jp))

### **Key Points:**

- Diffuse emission of whistler-mode waves from 1 Hz to 16 Hz is found over the polar regions of the moon in the solar wind.
- Right-hand polarized waves propagate parallel to the background magnetic field without a significant Doppler shift.
- The waves are thought to be generated by the ions reflected by the moon and propagate along field lines convected by the solar wind.

25

**26 Abstract**

27 The solar wind particles reflected by the lunar magnetic field are the major energy source of  
28 electromagnetic wave activities, such as the 100 s magnetohydrodynamic waves and the 1 Hz  
29 whistler-mode waves generated by protons and the non-monochromatic whistler-mode waves  
30 generated by mirror-reflected electrons. Kaguya found a new type of whistler-mode waves at 100  
31 km altitude above the polar regions of the moon with a broad frequency range of 1–16 Hz. The  
32 waves appear diffuse in both the time and frequency domains, and their occurrence is less  
33 sensitive to the magnetic connection to the lunar surface. The polarization is right-handed with  
34 respect to the background magnetic field, and the wave number vector is nearly parallel to the  
35 magnetic field perpendicular to the solar wind flow. The diffuse waves are thought to be  
36 generated by the solar wind ions reflected by the lunar magnetic field through cyclotron  
37 resonance. The resonant ions are expected to have a velocity component parallel to the magnetic  
38 field larger than the solar wind bulk speed; however, such ions were not always simultaneously  
39 detected by Kaguya. The waves may have been generated above the dayside of the moon and  
40 then propagated along the magnetic field being convected by the solar wind to reach the polar  
41 regions to be detected by Kaguya.

**42 Plain Language Summary**

43 Unlike Earth, the moon is not shielded by a global magnetic field; hence, solar wind particles can  
44 access the lunar surface. Although most of these particles are absorbed by the surface, a small  
45 fraction is scattered by the surface or reflected by intense lunar magnetic fields (magnetic  
46 anomalies) back into the solar wind and can become an energy source of wave activities. The  
47 protons reflected by these magnetic anomalies generate 0.01 Hz ultra-low frequency waves and 1  
48 Hz electron cyclotron waves. The electrons reflected by the lunar magnetic field form a field-  
49 aligned beam that generates broadband electromagnetic waves, whose detection depends on the  
50 magnetic connection of spacecraft to the lunar surface. Kaguya found a new type of  
51 electromagnetic waves with a broad frequency range like the waves generated by the electrons,  
52 but less sensitive to the magnetic connection like the waves generated by the reflected protons.  
53 These electromagnetic waves are preferentially observed above the polar region of the moon, not  
54 above intense magnetic anomalies. They are thought to be generated by the solar wind ions  
55 reflected by the lunar magnetic fields and propagate along the solar wind magnetic field to the  
56 polar region being convected down the solar wind flow.

57

58

59 **1 Introduction**

60 Solar wind particles directly hit the moon due to the lack of a global-scale magnetic field  
61 or a dense atmosphere. Most of them are absorbed by the lunar surface, leaving a plasma void,  
62 called a lunar wake, on the downstream side (Lyon et al., 1967; Colburn et al., 1967; Schubert &  
63 Lichtenstein, 1974; Bosqued et al., 1996; Ogilvie et al., 1996). A small fraction of these particles  
64 is scattered, reflected, or diffracted by the lunar surface or its crustal magnetic field.  
65 Observations from Kaguya and Chandrayaan-1 revealed that 0.1–1% of the incident plasmas is  
66 backscattered by the lunar surface, while 10–50% is reflected by the local crustal fields, called  
67 magnetic anomalies (Saito et al., 2008, 2010; Lue et al., 2011). Above intense magnetic  
68 anomalies, the deceleration of ions and the acceleration of electrons parallel to the magnetic field  
69 were observed together with heating of reflected ions (Saito et al., 2012). Chandrayaan-1 and  
70 IBEX showed that up to 20% of the incident solar wind particles is backscattered in the form of  
71 energetic neutral hydrogen atoms with energy of several tens of eV. Some of the particles  
72 experience charge exchange with ambient plasmas and begin to behave as reflected protons  
73 thereafter (McComas et al., 2009; Wieser et al., 2009, 2011; Poppe et al., 2014; Bhardwaj et al.,  
74 2015).

75 Backscattered, reflected, or diffracted particles are the main source of various wave  
76 activities (Harada et al., 2015; Nakagawa, 2016; Harada & Halekas, 2016, and references  
77 therein). The most prominent waves in the low-frequency range are the 0.01 Hz ultra-low-  
78 frequency waves (Nakagawa et al., 2012) and the 1 Hz whistler-mode waves (Halekas et al.,  
79 2006b; Tsugawa et al., 2011) generated by the reflected protons through cyclotron resonance  
80 with solar wind magnetohydrodynamic waves or the whistler-mode waves propagating against  
81 the solar wind flow. Figures 1a and 1b show typical examples of such waves. They are Doppler-  
82 shifted and detected as narrowband, often left-handed polarized waves with respect to the  
83 background magnetic field. Their occurrence is not sensitive to the magnetic connection between  
84 spacecraft and the lunar surface estimated from the intersection of the linearly extrapolated line  
85 of force of the magnetic field observed at Kaguya and the lunar surface. The red and blue bars at  
86 the bottom of each spectrum in Figure 1 indicate the magnetic connection to the dayside and  
87 nightside surfaces of the moon, respectively. The narrowband waves in Figures 1a and 1b were  
88 continuously observed, while the magnetic connection was intermittent. The detection was not  
89 controlled by the magnetic connection, suggesting that they were generated by protons with a  
90 large gyro radius.

91 Another kind of prominent wave found around the moon is the non-monochromatic  
92 whistler-mode waves in the extremely low frequency (ELF) range of 0.1 Hz to 10 Hz (Nakagawa  
93 et al., 2011; Tsugawa et al., 2012). They are often observed on the dayside of the moon, and their  
94 occurrence is severely controlled by the magnetic connection of spacecraft to the lunar surface.  
95 Figure 1c shows an example of a non-monochromatic whistler-mode wave. The broadband  
96 emission was mainly observed when Kaguya was magnetically connected to the dayside surface  
97 of the moon. The wave activity was reduced at around 3:08, 3:30, and 3:37–3:42 when the  
98 magnetic connection was lost and immediately recovered as the connection recovered. The wave  
99 intensity enhanced when the spacecraft was magnetically connected to the magnetic anomalies,  
100 suggesting that the energy source was the electrons bound to the magnetic field lines within a

101 small gyroradius. The waves are thought to be generated by the mirror-reflected electrons above  
 102 the lunar crustal magnetic field (Saito et al., 2012).

103 These low-frequency waves around the moon can be categorized into two types: (1)  
 104 monochromatic waves with a sharp boundary in the frequency domain not sensitive to the  
 105 magnetic connection to the lunar surface; and (2) non-monochromatic waves with a sharp  
 106 boundary in the time domain sensitive to the magnetic connection to the lunar surface. In  
 107 addition to these known waves, a new type of diffuse ELF wave was also found by Kaguya  
 108 above the polar region of the moon. It is a diffuse emission both in the frequency and time  
 109 domains. The waves appeared in a broad frequency range from 1 Hz to 16 Hz like the ELF  
 110 waves generated by the reflected electrons. However, different from that of the electron-  
 111 generated ELF waves, their occurrence was not sensitive to the magnetic connection to the lunar  
 112 surface like the waves generated by protons. Their generation mechanism is not known. This  
 113 paper reports the characteristics and the possible generation mechanism of the newly found  
 114 diffuse ELF waves.

## 115 **2 Data**

116 The magnetic field and the plasma data used in this study were obtained by Lunar  
 117 MAGnetometer (LMAG) and Plasma energy Angle and Composition Experiment (PACE) of the  
 118 MAGnetic field and Plasma experiment (MAP) (Saito et al., 2008, 2010; Tsunakawa et al., 2010;  
 119 Shimizu et al., 2008) onboard Kaguya on its polar orbit around the moon during the period from  
 120 January 1, 2008 to September 30, 2008. The spacecraft altitude was approximately 100 km  
 121 above the lunar surface (Kato et al., 2010). The period of orbital motion was approximately 2 h.

122 The magnetic field vectors obtained by the LMAG at 32 Hz sampling frequency  
 123 (Takahashi et al., 2009) were Fourier transformed every 32 s. Minimum variance analysis  
 124 (Sonnerup and Cahill, 1967) was applied to each Fourier component to obtain the direction of the  
 125 wavenumber vector  $\mathbf{k}$ . The  $\mathbf{k}$  vector was assumed to be parallel to the minimum direction. The  
 126 intermediate and maximum variance components were separated into left- or right-handed  
 127 polarized components with respect to the background magnetic field. The sense of rotation  
 128 (polarization) with respect to the background magnetic field of the wave is defined as  $(B_L^2 - B_R^2) /$   
 129  $(B_L^2 + B_R^2)$ , where  $B_L$  and  $B_R$  are the amplitudes of the left- or right-handed components,  
 130 respectively.

131 The three-dimensional (3D) energy distributions of the ions and the electrons were  
 132 obtained using four sensors of the MAP-PACE, Ion Energy Analyzer (IEA), and Ion Mass  
 133 Analyzer (IMA) for the ions and Electron Spectrum Analyzer (ESA)-S1 and ESA-S2 for the  
 134 electrons. The IMA and ESA-1 sensors were installed on the nadir-looking panel of the  
 135 spacecraft to detect the particles coming from the moon, while the IEA and ESA-2 sensors were  
 136 installed on the zenith-looking panel. The energy range was 7 eV/q–29 keV/q for the IEA, 7  
 137 eV/q–28 keV/q for the IMA, 6 eV–9 keV for the ESA-S1, and 9 eV–16 keV for the ESA-S2  
 138 (Saito et al., 2010). The densities of the ions observed by the IMA and the IEA were separately  
 139 calculated from each distribution function (Saito et al., 2010) and combined to obtain the total  
 140 ion density.

141 The upstream solar wind condition was monitored using Level 2 data from the Solar  
 142 Wind Electron, Proton, and Alpha Monitor (SWEPAM) onboard the Advanced Composition

143 Explorer (ACE) spacecraft. The data were extracted from the OMNI data set of NASA/GSFC  
144 through OMNIWeb Plus.

### 145 3 Observations

#### 146 3.1 Diffuse ELF waves in the solar wind

147 Figure 2 shows an example of the diffuse ELF waves found by Kaguya on March 8, 2008  
148 when the moon was in the solar wind (Figure 3a). A diffuse emission was observed in the  
149 frequency range of 4 Hz to 16 Hz during the period from 7:03 to 7:13 when the spacecraft was  
150 above the southern polar region of the moon (Figures 2f and 3c–d). In the previous spacecraft  
151 evolution, faint, but similar waves were seen from 5:11 to 5:17 in a range of 6–12 Hz in the same  
152 region over the south pole. The frequency range was between the ion and electron cyclotron  
153 frequencies of 0.075 Hz and 0.14 kHz (for the magnetic field of 4.9 nT at 7:05). The ion bulk  
154 density calculated from the velocity distribution functions from the IEA and the IMA was  
155 approximately  $8.0 \times 10^6 \text{ m}^{-3}$  during the period, which resulted in a lower hybrid frequency of 3.2  
156 Hz. The diffuse ELF wave frequency was close to the lower hybrid frequency. Figure 4 shows a  
157 comparison of the cross-cut spectrum of the power density of the diffuse wave (Figure 4b) with  
158 that for a quiet period (Figure 4a). The power density enhanced over a wide range from 4 Hz to  
159 16 Hz.

160 The diffuse waves were detected when Kaguya was not magnetically connected to the  
161 lunar surface, as indicated by the blanks in Figure 2b. The background magnetic field  $\mathbf{B}_0$  was  
162 almost in the  $y_{sse}$  direction of the selenocentric solar ecliptic (sse) coordinate system during the  
163 diffuse ELF wave detection (Figure 2g).

164 Figure 2c shows the sense of polarization in the spacecraft frame of reference for each  
165 Fourier component, whose power density was greater than  $5 \times 10^{-3} \text{ nT}^2/\text{Hz}$ . The red color in the  
166 figure indicates the right-handed polarization with respect to the background magnetic field. The  
167 diffuse ELF wave polarization was predominantly right-handed with respect to the background  
168 magnetic field. The wave number vector  $\mathbf{k}$  of the diffuse ELF wave was nearly parallel to the  
169 background magnetic field  $\mathbf{B}_0$ . Figure 2d shows the angle  $\theta_{\mathbf{k}, \mathbf{B}_0}$  between vectors  $\mathbf{k}$  and  $\mathbf{B}_0$ . The  
170 red color indicates that vector  $\mathbf{k}$  was parallel to  $\mathbf{B}_0$ . The polarization and propagation directions  
171 suggested that the diffuse ELF emissions were whistler-mode waves. No significant Doppler  
172 shift was expected because the  $\mathbf{k}$  vector was nearly perpendicular to the bulk flow of the solar  
173 wind in the  $x_{sse}$  direction (Figure 2e).

174 The diffuse waves were not detected above intense magnetic anomalies. Figure 5 shows  
175 the Kaguya position during the detection of the diffuse wave projected onto a color-coded map  
176 of the crustal magnetic field magnitude at the lunar surface calculated from the Kaguya  
177 observation (Tsunakawa et al., 2015). No intense magnetic field was found at the Kaguya  
178 position. Most of the intense magnetic anomalies extended sunward and equatorward of Kaguya.

179 As shown in Figure 2g, the diffuse ELF waves were observed on the positive gradient of  
180 the magnitude toward a lunar external magnetic enhancement (LEME, see Halekas et al., 2006a)  
181 with a peak magnitude at 7:13. The diffuse waves disappeared at the LEME peak. Another type  
182 of low-frequency wave was observed at around 0–4 Hz at the LEME. However, its properties of  
183 mixed polarization and direction of wave number vectors nearly perpendicular to the magnetic  
184 field were quite different from the diffuse ELF waves.

185            Figures 2h and 2i show the energy–time spectra of the ions detected by the IEA and the  
186 IMA sensors of the MAP–PACE, respectively. During the diffuse ELF wave detection, the IMA  
187 observed a bunch of protons reflected by a crustal field from 7:02 to 7:10 in the energy range of  
188 0.1 keV to 1 keV, but the start and end times of the reflected ions were not exactly the same as  
189 those of the diffuse ELF waves. The IEA consistently detected incident solar wind ions centered  
190 at 0.5 keV with the ACE observation of 330 km/s at  $1.52 \times 10^6$  km upstream in the solar wind  
191 shifted by approximately 1 h for traveling the distance. The upstream number density of the solar  
192 wind at the ACE was  $2 \times 10^7 \text{ m}^{-3}$ , which was higher than the nominal value of the solar wind.  
193 The IMA detected another bunch of reflected protons from 6:53 to 7:00, which were not  
194 accompanied by diffuse ELF waves.

### 195 3.2 Diffuse ELF waves in the magnetosheath

196            Figure 6 shows another diffuse ELF event found in Earth’s magnetosheath. Kaguya was  
197 on the nightside of the terminator, but was exposed to the magnetosheath flow (Figures 7c, 7d  
198 and 8). A diffuse emission was found in a frequency range from 1 Hz to 8 Hz during the period  
199 from 20:40 to 21:00 on June 14, 2008 above the northern polar region of the moon. The emission  
200 appeared diffuse both in the time and frequency domains, making a clear contrast with the  
201 broadband emissions with a sharp appearance and a mixed polarization observed from 21:00 to  
202 22:00.

203            The observed frequency of 1–8 Hz corresponded to 3–24 times of the ion cyclotron  
204 frequency of 0.34 Hz calculated from the magnitude of the background magnetic field of 19.4–  
205 22.1 nT. Figure 6 presents three lanes of falling tone starting at around 20:40, 20:45, and 20:50.  
206 The polarization was right-handed with respect to the background magnetic field, and the  $\mathbf{k}$   
207 vector was again nearly parallel to the magnetic field. The  $\mathbf{k}$  vector was nearly perpendicular to  
208 the bulk flow of the magnetosheath plasma (Figure 6e) because the magnetic field was almost in  
209 southward direction (Figure 6g). Thus, Doppler-shift effect was supposed to be small.

210            Throughout the diffuse ELF wave event, Kaguya was magnetically connected to the  
211 lunar surface (Figure 6b). Figure 8 shows how the line of force of the magnetic field at Kaguya  
212 was connected to the moon. The line of force of the magnetic field was connected to the lunar  
213 surface just below the spacecraft, where no intense crustal magnetic field was found. A cluster of  
214 intense crustal fields is instead seen at the lower latitude, upstream side (orange line pointing to  
215 the sun at the lower left) of the spacecraft. Figure 9 depicts the polar view in the Lambert  
216 azimuthal equal area projection.

217            The diffuse appearance and insensitiveness to the magnetic connection suggest that the  
218 emission was generated by ions. An attempt was made to search for the ions that would generate  
219 the waves in the energy–time spectrogram of the ions detected by the IMA (Figure 6i), but it was  
220 difficult to distinguish the reflected ions from the incident solar wind component because the  
221 latter also entered the IMA sensor of Kaguya on this orbit just behind the terminator. The ion  
222 energy typically ranged from 0.5 keV to 2.0 keV, consistent with the bulk speed of 400 km/s of  
223 the sheath flow calculated from the distribution functions obtained by the IMA and the IEA  
224 during the period of the diffuse ELF event. The number density of the ions calculated from the  
225 IEA and IMA observations was  $1 \times 10^7 \text{ m}^{-3}$ .

226

## 227 4 Discussion

### 228 4.1 Summary of observation

229 The properties of the diffuse ELF waves observed by Kaguya around the moon are  
230 summarized as follows:

- 231 1) The waves were magnetic fluctuations in a frequency range of 1 Hz to 16 Hz between the  
232 local ion and electron cyclotron frequencies.
- 233 2) The waves were right-hand polarized with respect to the background magnetic field.
- 234 3) The wave number vector was nearly parallel to the background magnetic field.
- 235 4) The waves were detected irrespective of the magnetic connection to the lunar surface.
- 236 5) The waves were preferentially observed in the polar region.

### 237 4.2 Possible explanation for the broad frequency range

238 Considering the frequency range and the right-handed polarization with respect to the  
239 background magnetic field, the diffuse ELF waves are thought to be whistler-mode waves  
240 propagating nearly parallel to the background magnetic field. The energy source is supposed to  
241 be the ions reflected by the crustal magnetic field, which have broader energy and angular  
242 distributions compared to the incident solar wind (Saito et al., 2010, 2012). They would form a  
243 ring-beam distribution in the velocity space that can generate whistler-mode waves through  
244 cyclotron resonance (Gary, 1991).

245 The broadband, diffuse emission is expected to be caused by the ineffectiveness of the  
246 Doppler shift. If the wave number vector  $\mathbf{k}$  is antiparallel to the solar wind velocity  $\mathbf{V}_{sw}$ , the  
247 resonant waves will be heavily Doppler-shifted, and the observed bandwidth would be narrowed  
248 with reversed polarization (Figure 10a). The dashed lines in Figure 10 represent the Doppler-  
249 shift relationship between the angular frequencies  $\omega$  in the solar wind frame and  $\omega_{OBS}$  in the  
250 spacecraft frame of reference

$$251 \quad \omega + \mathbf{k} \cdot \mathbf{V}_{sw} = \omega_{OBS}. \quad (1)$$

252 The polarization  $\omega$ , which is positive (negative) for the right-handed (left-handed) polarization,  
253 would be reversed if the  $\mathbf{k} \cdot \mathbf{V}_{sw}$  term is large. In contrast, if the wave number vector  $\mathbf{k}$  is nearly  
254 perpendicular to the solar wind flow, the term  $\mathbf{k} \cdot \mathbf{V}_{sw}$  would be small and would not narrow the  
255 bandwidth or reverse the polarization (Figure 10b).

256 The real resonance occurred at a higher frequency than that illustrated in Figure 10. The  
257 resonant conditions will be investigated in the next section by using the dispersion curves drawn  
258 with the parameters observed.

### 259 4.3 Dispersion relation and resonant condition

260 Figure 11 shows the dispersion relation  $\omega(k)$  of parallel propagating whistler-mode  
261 waves drawn with the parameters of the diffuse ELF event observed on July 14, 2008. The  
262 magnitude of the magnetic field was 22.1 nT at 20:58. The plasma density was assumed to be  
263 equal to the ion density  $1 \times 10^7 \text{ m}^{-3}$  calculated from the 3D velocity distribution functions  
264 obtained from the IEA and IMA sensors of the PACE. The observed 1–8 Hz frequency  
265 normalized by the ion cyclotron frequency of 0.34 Hz corresponded to 3–24  $\Omega_i$ . The wave  
266 number vector was assumed to be parallel to the background magnetic field.

267 The dashed lines in Figure 11 represent the Doppler-shift equation (Eq. (1)) for the upper  
 268 and lower boundaries of the observed frequency. The  $-100$  km/s of inclination was calculated  
 269 from the bulk speed of  $400$  km/s observed by the MAP-PACE on the assumption that the wave  
 270 was propagating away from the moon, and the  $\mathbf{k}$  vector was antiparallel to the background  
 271 magnetic field ( $5.6, -7.6, -20.0$ ) nT. The dispersion curve intersected the upper and lower  
 272 boundaries at  $(\omega, k) = (21 \Omega_i, 9 \times 10^3 \Omega_i c^{-1})$  and  $(2 \Omega_i, 3 \times 10^3 \Omega_i c^{-1})$ , respectively. Thus, the  
 273 whistler-mode wave frequency in the sheath flow frame was estimated to range from  $0.6$  Hz to  $7$   
 274 Hz, and the wavelength was between  $100$  km and  $300$  km.

275 In Figure 11, the cyclotron resonance condition of the reflected ions with velocity  $\mathbf{V}_R$

$$276 \quad \omega + \mathbf{k} \cdot \mathbf{V}_{sw} - \mathbf{k} \cdot \mathbf{V}_R = -\Omega_i \quad (2)$$

277 is represented by the gray solid lines with positive inclinations. Three lines represent the ions  
 278 with a parallel speed  $V_{\parallel} \equiv (\mathbf{k} \cdot \mathbf{V}_{sw} - \mathbf{k} \cdot \mathbf{V}_R) / |\mathbf{k}|$  of  $440$  km/s ( $1$  keV),  $620$  km/s ( $2$  keV), and  $760$   
 279 km/s ( $3$  keV) as a measure of the energy of the solar wind (or magnetosheath) protons. A line  
 280 with a very small inclination does not intersect the curve in a positive  $\omega$  range. That is, very  
 281 slow ions cannot be resonant with the whistler-mode waves. The line for the  $1$  keV ions  
 282 intersects the dispersion curve at two points around  $1 \Omega_i$  and  $4 \Omega_i$ , and the latter agrees with the  
 283 observed frequency range. This is different from the illustrations in Figure 10, in which the  
 284 resonance is assumed to be at a lower frequency. The lower limit of the possible intersection  
 285 would be at around  $2 \Omega_i$ , consistent with the lowest frequency of the detected diffuse ELF waves  
 286 in the sheath flow frame.

287 To account for the upper boundary of the observed frequency, we need  $V_{\parallel}$  as large as  $760$   
 288 km/s ( $3$  keV), which is approximately  $\sqrt{3}$  times faster than the solar wind bulk speed. In Figure  
 289 6i, the upper boundary of the ion energy was approximately  $2$  keV in the spacecraft frame of  
 290 reference. The reflected ions with velocity  $\mathbf{V}_R$  in the spacecraft frame had velocity  $\mathbf{V}_R - \mathbf{V}_{sw}$  in  
 291 the solar wind (or magnetosheath flow) frame of reference. However, in this event, the wave  
 292 number vector  $\mathbf{k}$  is nearly perpendicular to the solar wind flow, and the term  $\mathbf{k} \cdot \mathbf{V}_{sw}$  does not  
 293 contribute to  $V_{\parallel}$ . The reflected ions must have a higher velocity than the solar wind speed to have  
 294 the parallel component  $V_{\parallel}$  as estimated.

295 Figure 6 shows a falling tone structure of the diffuse ELF waves. The magnetic field,  
 296 plasma density, and bulk velocity were stable during the period. Any distinct feature, which  
 297 might correspond to the falling tone structure, was searched for in the MAP-PACE data, but no  
 298 such feature was found. The frequency decrease can be interpreted as a decrease in the parallel  
 299 velocity component of the reflected ions responsible for the wave generation. Whether it was  
 300 temporal or spatial variation remains unclear. During the  $5$  min interval of the three lanes of  
 301 falling tone, Kaguya traveled approximately  $15^\circ$  in longitude. The direction of the velocities of  
 302 the reflected ions may have varied depending on the distance from their reflection point, but it is  
 303 not understood why the falling tone repeatedly appeared.

304 Figure 12 depicts the Doppler-shift relation of the observed frequencies overlaid on a  
 305 dispersion relation  $\omega(k)$  of the parallel propagating whistler wave for the March 8, 2008 diffuse  
 306 ELF event. The plasma density was assumed to be equal to the ion density  $8 \times 10^6 \text{ m}^{-3}$  calculated  
 307 from the velocity distribution measurements by the IEA and the IMA. The magnetic field  
 308 magnitude of  $4.9$  nT at  $07:05$  was employed. The observed frequency  $4$ – $16$  Hz normalized by the

309 ion cyclotron frequency of  $0.075 \text{ Hz}$  corresponded to  $54\text{--}210 \Omega_i$ . Note that the upper boundary  
 310 of the frequency range was limited by half of the sampling rate ( $32 \text{ Hz}$ ) of the magnetic field  
 311 observation.

312 The Doppler shift was small for this case. The bulk velocity of the solar wind calculated  
 313 from the MAP–PACE observation was  $250 \text{ km/s}$ , and the velocity component parallel to the  
 314 background magnetic field ( $0.47, 4.6, 1.5 \text{ nT}$ ) was as small as  $24 \text{ km/s}$ . The lines of the Doppler-  
 315 shift equation (Eq. (1)) with positive and negative inclinations were drawn for two possible  
 316 propagation directions parallel or antiparallel to the magnetic field. The frequency in the solar  
 317 wind frame fell in the range from  $54 \pm 8 \Omega_i$  ( $4 \pm 0.3 \text{ Hz}$ ) to  $210 \pm 10 \Omega_i$  ( $16 \pm 0.75 \text{ Hz}$ ). The wave  
 318 number  $|\mathbf{k}|$  was estimated to be  $6 \times 10^4 |\Omega_i|/c - 1.2 \times 10^5 |\Omega_i|/c$ , corresponding to the  
 319 wavelength from  $66 \text{ km}$  to  $33 \text{ km}$ .

320 The gray lines in Figure 12 depict the cyclotron resonance conditions for the ions with  
 321 three different values of  $V_{\parallel} = 310 \text{ km/s}$  ( $0.5 \text{ keV}$ ),  $440 \text{ km/s}$  ( $1 \text{ keV}$ ), and  $540 \text{ km/s}$  ( $1.5 \text{ keV}$ ). To  
 322 account for the observed frequency range, the ions should have velocity components  $V_{\parallel}$  in the  
 323 range of  $310 \text{ km/s}$ – $540 \text{ km/s}$ , which is approximately  $1\text{--}\sqrt{3}$  times larger than that of the incident  
 324 solar wind.  
 325

#### 326 4.4 Possible generation mechanism

327 The velocity component  $V_{\parallel}$  of the reflected ions must be larger than the solar wind bulk  
 328 speed to be resonant with the observed waves. On the contrary, in a magnetic field perpendicular  
 329 to the solar wind flow, the velocity component  $V_{\parallel}$  cannot exceed the incident speed. The speed of  
 330 the reflected ions can be two times as large as the incident speed in the solar wind frame of  
 331 reference, but it contributes a perpendicular component  $V_{\perp}$ , not a parallel component  $V_{\parallel}$ . The  
 332 parallel component  $V_{\parallel}$  is maximized when the ions are reflected into the direction parallel to the  
 333 magnetic field with the same speed as the initial speed. We need an initial speed larger than the  
 334 solar wind bulk speed to obtain fast enough  $V_{\parallel}$ . High-energy components and the core  
 335 component of the solar wind ions must be reflected into the magnetic field direction.

336 Another possibility is that the diffuse waves were generated in the upstream flow, not at  
 337 the Kaguya position. Figure 2i shows a slight disagreement in the appearance/disappearance time  
 338 between the diffuse waves and the reflected ions. Bunches of reflected protons at around 6:55  
 339 and 4:55 were not accompanied by the diffuse ELF waves. In Figures 8 and 9, we can hardly find  
 340 magnetic anomalies that would reflect incident ions. The ions responsible for the diffuse wave  
 341 generation might not be detected at the Kaguya position.

342 Figure 13 schematically illustrates the wave generation and propagation. The solar wind  
 343 ions reflected by the lunar magnetic field can have a large velocity component  $V_{\perp}$  perpendicular  
 344 to the magnetic field (Saito et al., 2010) and a large gyroradius (Nishino et al., 2009, 2013). A  
 345 whistler-mode wave was generated in the upstream solar wind by the reflected ions and began  
 346 propagating along the magnetic field line convected by the solar wind flow. The slower wave  
 347 components might crash into the lunar surface before they reach the limb. Only the wave  
 348 component that is fast enough can propagate to the limb (polar region or the terminator) to be  
 349 detected by Kaguya. The group velocity of the whistler-mode wave is higher than the phase

350 velocity that determines the resonant condition; hence, the resonant ions may not reach Kaguya  
351 above the polar region. The ions might hit the moon to be absorbed by the surface or reflected by  
352 the lunar magnetic field again into directions that are different from those of the wave. Multiple  
353 reflections might increase the ion velocity by the self-pickup process (Saito et al., 2010).  
354

## 355 **5 Conclusions**

356 Diffuse, right-hand polarized whistler-mode waves propagating parallel to the magnetic  
357 field were found by Kaguya over the polar regions of the moon. These waves are thought to be  
358 generated by the solar wind ions reflected by the lunar magnetic field into directions  
359 perpendicular to the solar wind flow. Due to ineffectiveness of the Doppler shift, the polarization  
360 was not reversed, and the frequency range was not narrowed. The reflected ions resonant with  
361 the whistler-mode waves must have a higher velocity component parallel to the magnetic field  
362 than the solar wind bulk speed, although such higher-energy ions were not always  
363 simultaneously detected. A possible explanation for this is that the cyclotron resonance occurs  
364 upstream in the solar wind above the lunar magnetic anomaly, and the waves propagate along the  
365 magnetic field to the polar region during the travel time of the solar wind to pass from the  
366 resonant site to the observer at the polar region.

## 367 **Acknowledgments**

368 The authors thank the Kaguya MAP-LMAG and MAP-PACE teams for the Kaguya  
369 magnetic field and plasma particle data. The Kaguya MAP-LMAG and MAP-PACE data are  
370 available at Kaguya (SELENE) Data Archive (<http://l2db.selene.darts.isas.jaxa.jp/index.html.en>).  
371 The authors also thank the ACE SWEPAM instrument team and the ACE Science Center for  
372 providing the ACE data. Interplanetary magnetic field parameter (MAG) and solar wind  
373 parameter (SWEPAM) data obtained by ACE are available at the ACE Science Center  
374 (<http://www.srl.caltech.edu/ACE/ASC/index.html>). T. Nakagawa thanks Yoshiki Sugata and Sho  
375 Ito for their contribution in event finding and examination of spatial distribution and solar wind  
376 condition. The authors declare that they have no conflicts of interests. This work was supported  
377 by JSPS KAKENHI Grant Number 18K03727.

## 378 **References**

- 379 Bhardwaj, A., Dhanya, M. B., Alok1, A., Barabash, S., Wieser, M., Futaana, Y., Wurz, P.,  
380 Vorburger, A., Holmström, M., Lue, C., Harada, Y., & Asamura, K. (2015), A new view  
381 on the solar wind interaction with the Moon, *Geosci. Lett.* 2:10, DOI 10.1186/s40562-  
382 015-0027-y.
- 383 Bosqued, J. M., Lormant, N., R`eme, H., d'Uston, C., Lin, R. P., Anderson, K. A., Carlson, C.  
384 W., Ergun, R. E., Larson, D., McFadden, J., McCarthy, M. P., Parks, G. K., Sanderson,  
385 T. R., & Wenzel, K.-P. (1996), Moon solar wind interaction: First results from the  
386 WIND/3DP experiment, *Geophys. Res. Lett.*, 23, 1259–1262, doi:10.1029/96GL00303.
- 387 Colburn, D.S., R. G. Currie, J. D. Mihalov, C. P. Sonett (1967), Diamagnetic solar-wind cavity  
388 discovered behind moon, *Science*, 158, 1040–1042.
- 389 Gary, S. P. (1991), Electromagnetic ion/ion instabilities and their consequences in space plasmas  
390 - A review, *Space Science Reviews*, 56, p. 373 – 415, doi:10.1007/BF00196632.

- 391 Halekas, J. S., Brain, D. A., Mitchell, D. L., Lin, R. P., Harrison, L. (2006a), On the occurrence  
392 of magnetic enhancements caused by solar wind interaction with lunar crustal fields.  
393 *Geophys. Res. Lett.* 33, L01201, doi:10.1029/2006GL025931.
- 394 Halekas, J. S., Brain, D. A., Mitchell, D. L., & Lin, R. P. (2006b), Whistler waves observed near  
395 lunar crustal magnetic sources. *Geophysical Research Letters*, 33, L22104.  
396 doi:10.1029/2006GL027684.
- 397 Harada, Y., Halekas, J. S., Poppe, A. R., Tsugawa, Y., Kurita, S., & McFadden, J. P. (2015),  
398 Statistical characterization of the forenoon particle and wave morphology: ARTEMIS  
399 observations. *J. Geophys. Res. Space Physics*, 120, 4907–4921. doi:  
400 10.1002/2015JA021211.
- 401 Harada, Y., & Halekas, J. S. (2016), Upstream Waves and Particles at the Moon, in *Low-*  
402 *Frequency Waves in Space*, chap. 18, pp. 307–322, John Wiley Sons, Inc, Hoboken, NJ,  
403 doi: 10.1002/9781119055006.
- 404 Kato, M., Sasaki, S., Takizawa, Y. & the Kaguya project team (2010), The Kaguya mission  
405 overview, *Space Sci. Rev.*, 154, 3–19, doi:10.1007/s11214-010-9678-3.
- 406 LRO Project and Lunar Geodesy and Cartography Working Group (2008), A standardized lunar  
407 coordinate system for the Lunar Reconnaissance Orbiter and lunar datasets, LRO Project  
408 and LGCWG White Paper, version 5, Goddard Space Flight Center, National Aeronautics  
409 and Space Administration, <http://lunar.gsfc.nasa.gov/library/LunCoordWhitePaper-10-08.pdf>.
- 410 Lyon, E. F., Bridge, H. S., & Binsack, J. H. (1967), Explorer 35 plasma measurements in the  
411 vicinity of the Moon, *J. Geophys. Res.*, 72(23), 6113–6117,  
412 doi:10.1029/JZ072i023p06113.
- 413 Lue, C., Futaana, Y., Barabash, S., Wieser, M., Holmström, M., Bhardwaj, A., Dhanya, M.  
414 B., & Wurz, P. (2011), Strong influence of lunar crustal fields on the solar wind flow,  
415 *Geophys. Res. Lett.*, 38, L03202, doi:10.1029/2010GL046215.
- 416 McComas, D. J., Allegrini, F., Bochsler, P., Frisch, P., Funsten, H. O., Gruntman, M., Janzen, P.  
417 H., Kucharek, H., Möbius, E., Reisenfeld, D. B., & Schwadron, N. A. (2009), Lunar  
418 backscatter and neutralization of the solar wind: First observations of neutral atoms from  
419 the Moon, *Geophys. Res. Lett.*, 36, DOI: 10.1029/2009GL038794.
- 420 Nakagawa, T. (2016), ULF/ELF waves in the near-Moon space, in *Low-Frequency Waves in*  
421 *Space*, chap. 17, pp. 295–306, John Wiley Sons, Inc, Hoboken, NJ,  
422 doi:10.1002/9781119055006.
- 423 Nakagawa, T., Takahashi, F., Tsunakawa, H., Shibuya, H., Shimizu, H., & Matsushima, M.  
424 (2011). Non-monochromatic whistler waves detected by Kaguya on the dayside surface  
425 of the moon. *Earth, Planets and Space*, 63, 37–46, doi:10.5047/eps.2010.01.005
- 426 Nakagawa, T., Nakayama, A., Takahashi, F., Tsunakawa, H., Shibuya, H., Shimizu, H., &  
427 Matsushima, M. (2012). Large-amplitude monochromatic ULF waves detected by  
428 Kaguya at the moon. *Journal of Geophysical Research*, 117, A04101,  
429 doi:10.1029/2011JA017249.
- 430 Nishino, M. N., Fujimoto, M., Maezawa, K., Saito, Y., Yokota, S., Asamura, K., Tanaka, T.,  
431 Tsunakawa, H., Matsushima, M., Takahashi, F., Terasawa, T., Shibuya, H., Shimizu, H.

- 432 (2009) Solar-wind proton access deep into the near-Moon wake, *Geophys. Res. Lett.*, 36,  
433 L16103, doi:10.1029/2009GL039444.
- 434 Nishino, M. N., Fujimoto, M., Saito, Y., Tsunakawa, H., Kasahara, Y., Kawamura, M.,  
435 Matsushima, M., Takahashi, F., Shibuya, H., Shimizu, H., Goto, Y., Hashimoto, K.,  
436 Omura, Y., Kumamoto, A., Ono, T., Yokota, S. (2013) Type-II entry of solar wind  
437 protons into the lunar wake: Effects of magnetic connection to the night-side surface,  
438 *Planetary and Space Science*, 87, 106-114, doi:10.1016/j.pss.2013.08.017.
- 439 Ogilvie, K. W., Steinberg, J. T., Fitzenreiter, R. J., Owen, C. J., Lazarus, A. J., Farrell, W. M.,  
440 Torbert, R. B. (1996), Observation of the lunar plasma wake from the WIND spacecraft  
441 on December 27, 1994, *Geophys. Res. Lett.*, 23, 1255-1258, doi:10.1029/96GL01069.
- 442 Poppe, A. R., Sarantos, M. Halekas, J. S., Delory, G. T., Saito, Y. Nishino, M. (2014),  
443 Anisotropic solar wind sputtering of the lunar surface induced by crustal magnetic  
444 anomalies, *Geophys. Res. Lett.*, 41, 4865–4872, doi:10.1002/2014GL060523.
- 445 Saito, Y., S. Yokota T. Tanaka K. Asamura M. N. Nishino M. Fujimoto H. Tsunakawa H. Shibuya  
446 M. Matsushima H. Shimizu F. Takahashi T. Mukai T. Terasawa, (2008), Solar wind  
447 proton reflection at the lunar surface: Low energy ion measurement by MAP-PACE  
448 onboard SELENE (Kaguya), *Geophys. Res. Lett.*, 35, L24205,  
449 doi:10.1029/2008GL036077.
- 450 Saito, Y., Yoshifumi Saito, Yokota, S., Asamura, K., Tanaka, T., Nishino, M. N., Yamamoto, T.,  
451 Terakawa, Y., Fujimoto, M., Hasegawa, H., Hayakawa, H., Hirahara, M., Hoshino, M.,  
452 Machida, S., Mukai, T., Nagai, T., Nagatsuma, T., Nakagawa, T., Nakamura, M., Oyama,  
453 K.-I., Sagawa, E., Sasaki, S., Seki, K., Shinohara, I., Terasawa, T., Tsunakawa, H.,  
454 Shibuya, H., Matsushima, M., Shimizu, H., & Takahashi, F. (2010), In-flight performance  
455 and initial results of Plasma energy Angle and Composition Experiment (PACE) on  
456 SELENE (Kaguya), *Space Sci. Rev.*, 154, 265-303, doi:10.1007/s11214-010-9647-x.
- 457 Saito, Y., Nishino, M. N., Fujimoto, M., Yamamoto, T., Yokota, S., Tsunakawa, H., Shibuya, H.,  
458 Matsushima, M., Shimizu, H. & Takahashi, F. (2012), Simultaneous observation of the  
459 electron acceleration and ion deceleration over lunar magnetic anomalies, *Earth Planet.*  
460 *Space*, 64(2), 83-92, doi:10.5047/eps.2011.07.011.
- 461 Schubert, G. & Lichtenstein, B. R. (1974), Observations of moon-plasma interactions by orbital  
462 and surface experiments, *Rev. Geophys. Space Phys.*, 12, 592-626.
- 463 Shimizu, H., Takahashi, F., Horii, N., Matsuoka, A., Matsushima, M., Shibuya, H., &  
464 Tsunakawa, H. (2008), Ground calibration of the high-sensitivity SELENE lunar  
465 magnetometer LMAG. *Earth, Planets and Space*, 60, 353–363, doi:10.1186/BF03352800.
- 466 Sonnerup, B. U. Ö. & Cahill, L. J. (1967), Magnetopause structure and attitude from Explorer 12  
467 observations, *J. Geophys. Res.*, 72(1), 171– 183, doi:10.1029/JZ072i001p00171.
- 468 Takahashi, F., Shimizu, H., Matsushima, M., Shibuya, H., Matsuoka, A., Nakazawa, S., Iijima,  
469 Y., Otake, H., & Tsunakawa, H. (2009). In-orbit calibration of the lunar magnetometer  
470 onboard SELENE (KAGUYA). *Earth, Planets and Space*, 61, 1269–1274.
- 471 Tsugawa, Y., Terada, N., Katoh, Ono, T., Tsunakawa, H., Takahashi, F., Shibuya, H., Shimizu,  
472 H., & Matsushima, M. (2011), Statistical analysis of monochromatic whistler waves near

- 473 the Moon detected by Kaguya, *Ann. Geophys.*, 29, 889–893, doi:10.5194/angeo-29-889-  
474 2011.
- 475 Tsugawa, Y., Katoh, Y., Terada, N., Y., Ono, T., Tsunakawa, H., Takahashi, F., Shibuya, H.,  
476 Shimizu, H., Matsushima, M., Saito, Y., Yokota, S., & Nishino, M. N. (2012), Statistical  
477 study of broadband whistler-mode waves detected by Kaguya near the Moon, *Geophys.*  
478 *Res. Lett.*, 39, L16101, doi:10.1029/2012GL052818.
- 479 Tsunakawa, H., Shibuya, H., Takahashi, F., Shimizu, H., Matsushima, M., Matsuoka, A.,  
480 Nakazawa, S., Otake H., & Iijima Y. (2010), Lunar magnetic field observation and initial  
481 global mapping of lunar magnetic anomalies by MAP-LMAG onboard SELENE  
482 (Kaguya), *Space Sci. Rev.*, 154, 219-251, doi:10.1007/s11214-010-9652-0.
- 483 Tsunakawa, H., F. Takahashi, H. Shimizu, H. Shibuya, and M. Matsushima (2015), Surface  
484 vector mapping of magnetic anomalies over the Moon using Kaguya and Lunar  
485 Prospector observations, *J. Geophys. Res. Planets*, 120, 1160–1185,  
486 doi:10.1002/2014JE004785.
- 487 Wieser, M., Barabash, S., Futaana, Y., Holmström, M., Bhardwaj, A., Sridharan, R., Dhanya,  
488 M.B., Wurz, P., Schaufelberger, A., Asamura, K. (2009), Extremely high reflection of  
489 solar wind protons as neutral hydrogen atoms from regolith in space, *Planet. Space Sci.*,  
490 57, 2132-2134, doi:10.1016/j.pss.2009.09.012.
- 491 Wieser, M., Barabash, S., Futaana, Y., Holmström, M., Bhardwaj, A., Sridharan, R., Dhanya,  
492 M.B., Wurz, P., Schaufelberger, A., Asamura, K. (2011), Erratum to “Extremely high  
493 reflection of solar wind protons as neutral hydrogen atoms from regolith in space”,  
494 *Planet. Space Sci.*, 57, 798-799, doi:10.1016/j.pss.2011.01.016.  
495

496 **Figure Captions**

497 **Figure 1.** Examples of the low-frequency waves detected by Kaguya at 100 km altitude above  
 498 the lunar surface. (a) Ultra-low-frequency waves at 0.010–0.012 Hz and (b) whistler-mode  
 499 waves at 1.1–1.4 Hz generated by the reflected ions. (c) Non-monochromatic extremely low-  
 500 frequency waves generated by the reflected electrons. The red (blue) bars at the bottom of each  
 501 spectrum indicate that the linearly extrapolated line of force of the magnetic field at the  
 502 spacecraft intersects the dayside (nightside) surface of the moon.

503 **Figure 2.** Diffuse ELF waves observed by Kaguya at 100 km altitude above the moon on March  
 504 8, 2008. (a) Power density of the magnetic fluctuation. (b) Magnetic connection of Kaguya to the  
 505 nightside (blue) or dayside (red) surface of the moon estimated by the linear extrapolation of the  
 506 line of force of the magnetic field at Kaguya. (c) Sense of rotation of the magnetic field variation  
 507 with respect to the background magnetic field (red for right-hand and blue for left-hand), (d) the  
 508 angle between the  $\mathbf{k}$  vector and the background magnetic field  $\mathbf{B}_0$  for the Fourier components  
 509 with a power density larger than  $5 \times 10^{-3}$  nT<sup>2</sup> / Hz . (e) Angle between the  $\mathbf{k}$  vector and the  $x_{sse}$   
 510 axis of the selenocentric solar ecliptic (sse) coordinate system. (f) Position of Kaguya (  
 511  $x_{sse}, y_{sse}, z_{sse}$ ) together with the distance  $\sqrt{y_{sse}^2 + z_{sse}^2}$  from the  $x_{sse}$  axis. (g) 32 s-averaged  
 512 background magnetic field. (h) Omni-directional energy–time spectrogram of the ions from the  
 513 IEA sensor of the PACE looking at the zenith direction and (i) from the IMA sensor facing the  
 514 lunar surface.

515 **Figure 3.** Kaguya’s position at the diffuse ELF wave detection on March 8, 2008. (a) Position of  
 516 the moon in geocentric solar ecliptic (gse) coordinates. (b–d) Kaguya’s position projected on the  
 517 (b) x–y, (c) x–z, and (d) y–z planes of the selenocentric solar ecliptic (sse) coordinate system.

518 **Figure 4.** Spectra of the magnetic field variation observed by Kaguya around the moon on  
 519 March 8, 2008. (a) Quiet period from 6:30:22 to 6:30:54. (b) Diffuse ELF wave period from  
 520 7:08:12 to 7:08:44. The black curves are the power density resulting from the Fourier transform  
 521 applied for every 32 s of 32 Hz magnetic field data. The red lines depict the linear fit to the  
 522 observed spectra in the low-frequency range from 0.031 Hz to 1 Hz. The power density of the  
 523 higher-frequency range in panel (a) gives the noise level measurement. The enhancements in  
 524 panel (b) over the frequency range from 4 Hz to 16 Hz are significantly higher than the noise  
 525 level.

526 **Figure 5.** Kaguya’s position during the diffuse ELF wave event on March 8, 2008 projected onto  
 527 the map of the lunar crustal magnetic field. The colors indicate the magnetic field magnitude at 0  
 528 km altitude (Tsunakawa et al., 2015) on the Lambert azimuthal equal area projection. Kaguya’s  
 529 position (red crosses) is plotted every 1 min from 5:11 to 5:17 and 7:03 to 7:13.

530 **Figure 6.** A diffuse ELF event observed by Kaguya on June 14, 2008. See the legend of Figure  
 531 2.

532 **Figure 7.** Kaguya’s position at the diffuse ELF wave detection on June 14, 2008. (a) Position of  
 533 the moon in geocentric solar ecliptic (gse) coordinates. (b–d) Kaguya’s position projected on the  
 534 (b) x–y, (c) x–z, and (d) y–z planes of the sse coordinate system.

535

536 **Figure 8.** Magnetic connection between Kaguya and the lunar surface at 20:50 on June 14, 2008.  
 537 Kaguya is represented by a cube (not in scale). The line of force of the magnetic field observed  
 538 at Kaguya is represented by a purple bar extending from Kaguya. The magnetic connection to the  
 539 lunar surface is examined. The red, green, and blue lines indicate the  $x_{\text{ME}}$ ,  $y_{\text{ME}}$ , and  $z_{\text{ME}}$  axes,  
 540 respectively, of the mean Earth/Polar Axis (ME) reference system, in which the  $x_{\text{ME}}$  axis is  
 541 defined by the mean Earth direction, and the  $z_{\text{ME}}$  axis is defined by the mean rotational pole  
 542 (LRO Project and LGCWG, 2008). The orange line extending from the equator to the lower left  
 543 direction indicates the Sun's direction. The lunar surface is color-coded with the magnitude of  
 544 the lunar crustal field at 0 km altitude (Tsunakawa et al., 2015).

545 **Figure 9.** Kaguya's position and the lunar crustal magnetic field on the northern hemisphere at 0  
 546 km altitude (Tsunakawa et al., 2015). Kaguya's position from 20:40 to 20:59 is plotted every 1  
 547 min on the Lambert azimuthal equal area projection.  
 548

549 **Figure 10.** Schematic of the observed bandwidth of the Doppler-shifted waves. The curves represent the  
 550 dispersion diagrams for the plasma waves in the extremely low-frequency range with a positive  $\omega$  for the  
 551 right-hand polarized waves and a negative  $\omega$  for the left-hand polarized waves propagating parallel to the  
 552 background magnetic field. The solid lines depict the cyclotron resonance conditions. The dashed lines  
 553 represent the Doppler shifts. In (a) the heavily Doppler-shifted case, the bandwidth is narrowed, and  
 554 the polarization is reversed. In (b) the slightly Doppler-shifted case, the bandwidth remains broad, and  
 555 the polarization remains right-handed.  
 556

557 **Figure 11.** Dispersion relation of the whistler-mode wave, cyclotron resonance condition, and Doppler  
 558 shift relation for the diffuse ELF waves on 20:58 of June 14, 2008. The angular frequency is normalized  
 559 by the magnitude of the ion cyclotron frequency  $|\Omega_i|$ . The wave number is normalized by  $|\Omega_i|/c$ ,  
 560 where  $c$  is the speed of light.  
 561

562 **Figure 12.** Dispersion diagram, cyclotron resonance condition, and Doppler shift for the diffuse ELF  
 563 waves on 7:05 of March 8, 2008. See the legend of Figure 11.  
 564

565 **Figure 13.** Schematic of the whistler-mode wave propagating parallel to the magnetic field convected by  
 566 the solar wind. The reflected ion trajectory is not in the exact direction. The position and size of  
 567 Kaguya are not in scale.

Figure 1.

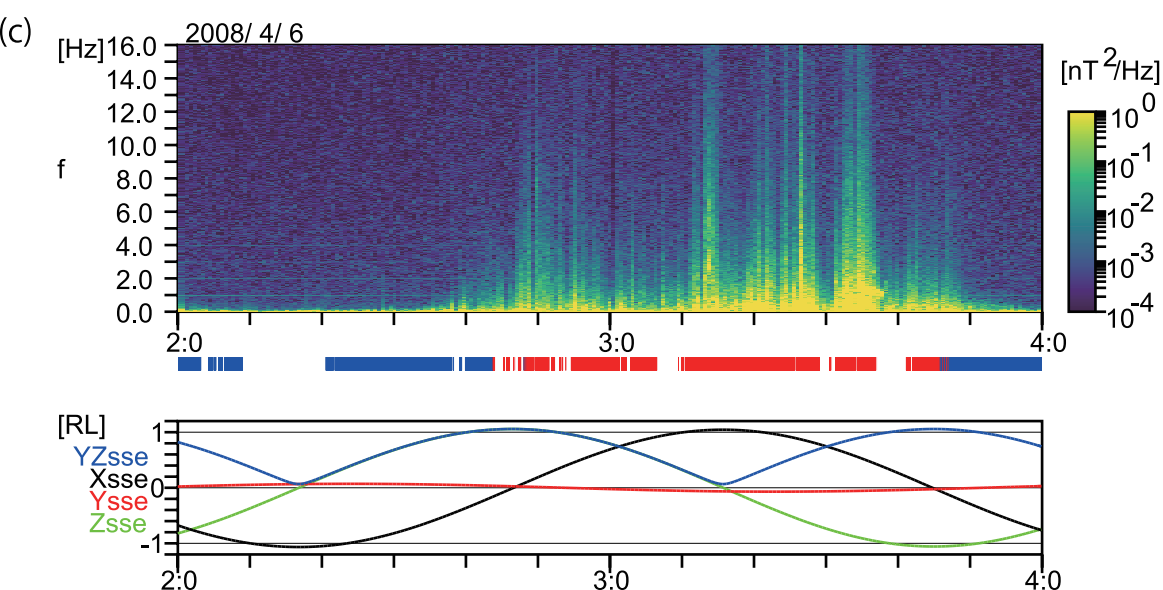
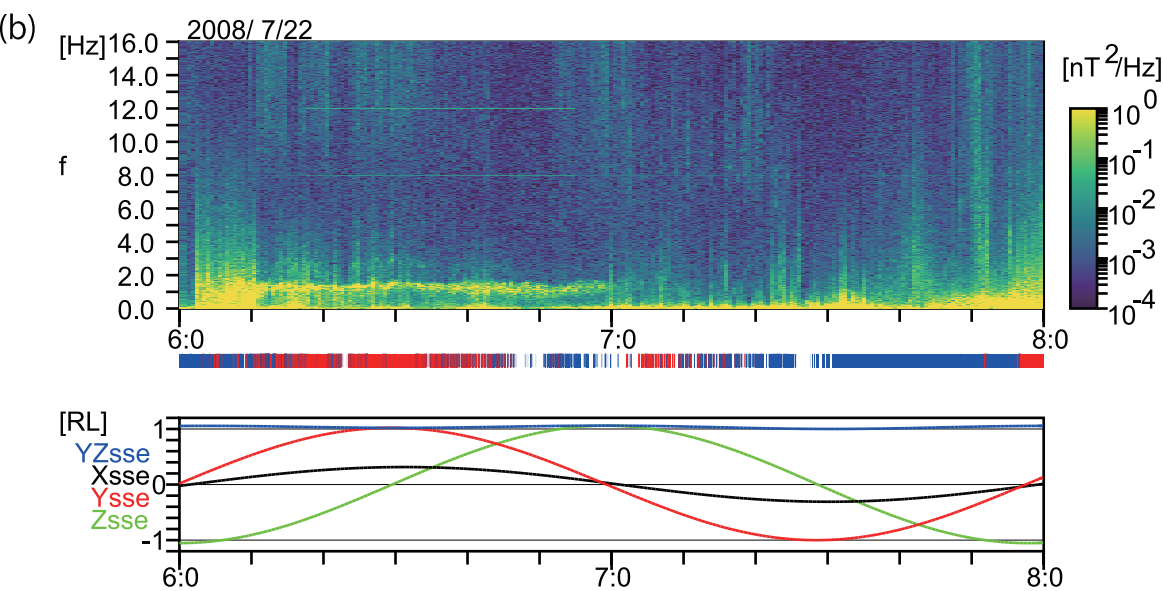
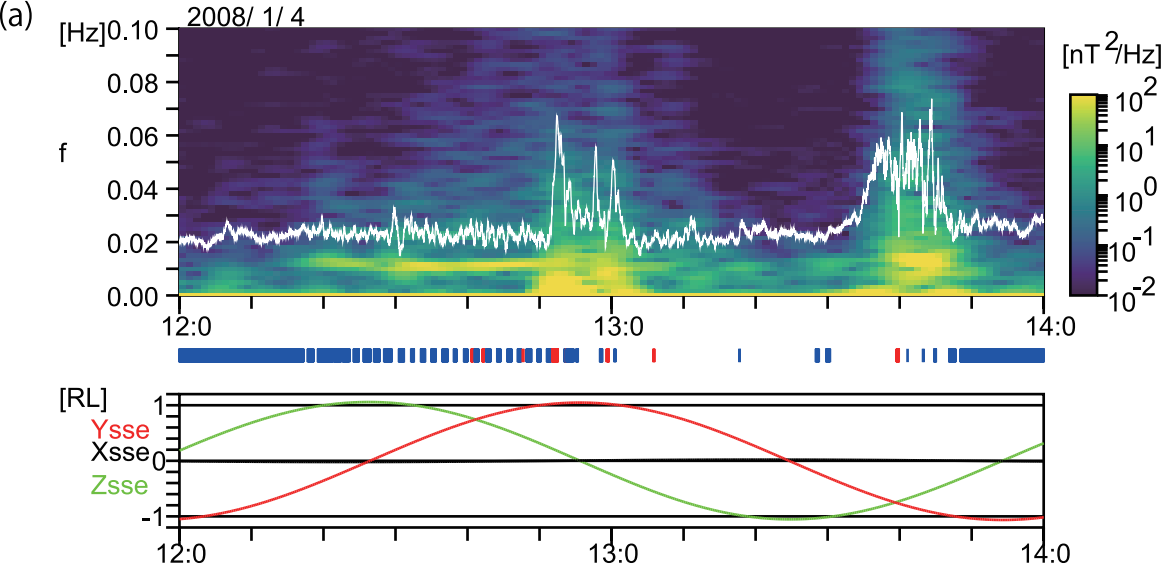


Figure 2.

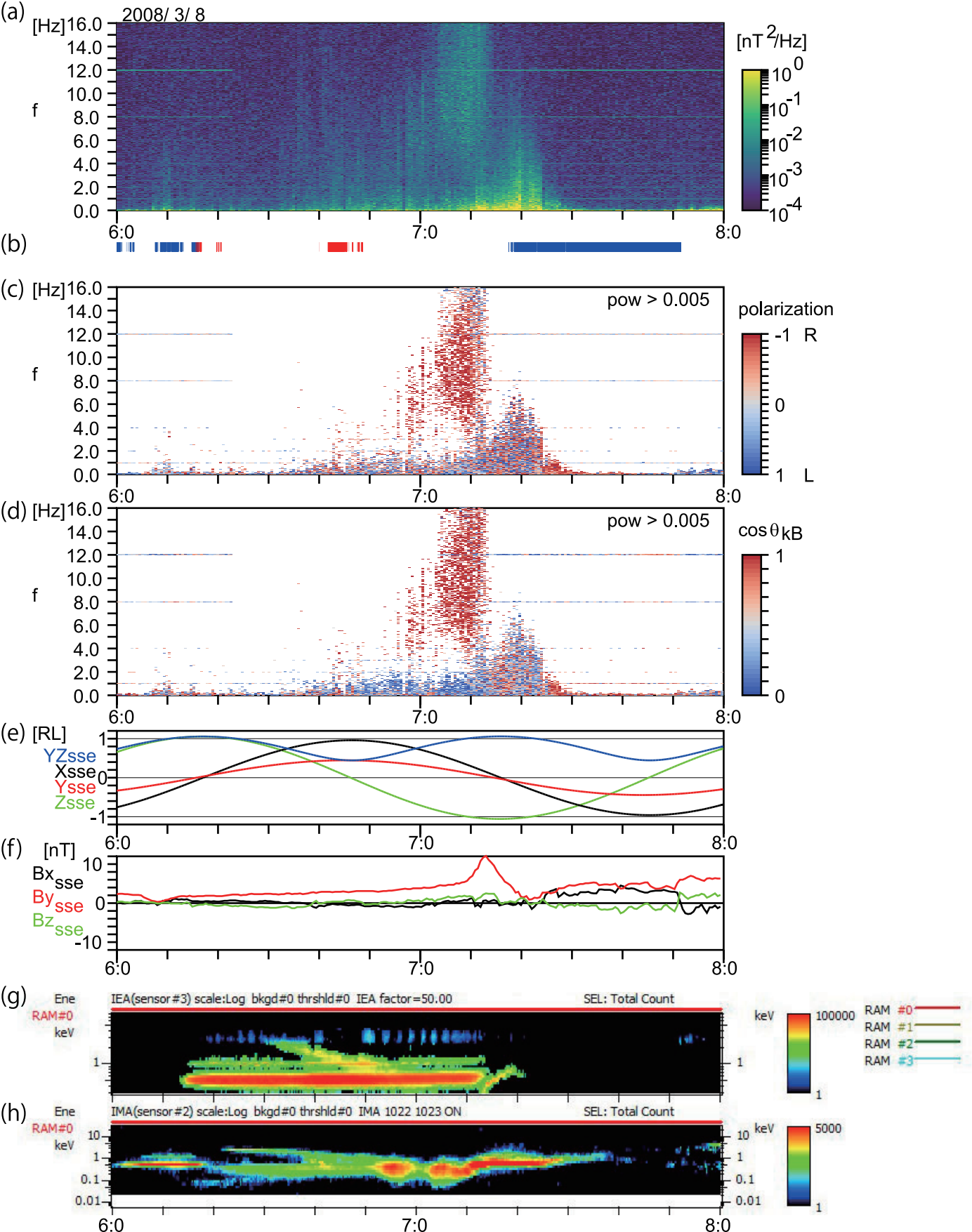
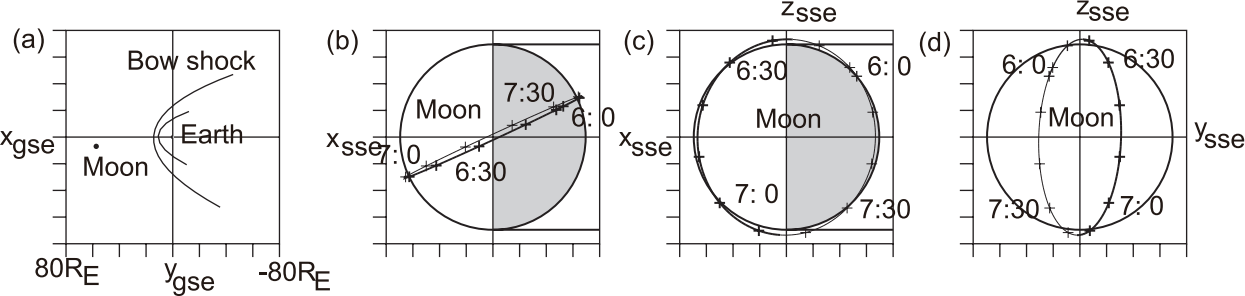


Figure 3.



**Figure 4.**

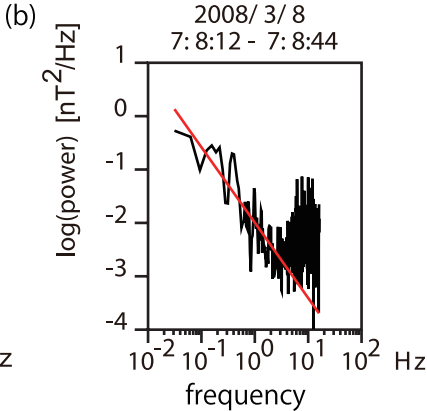
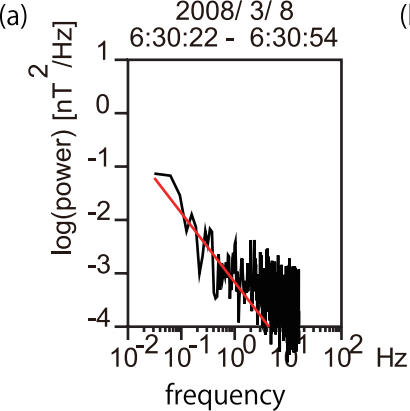


Figure 5.

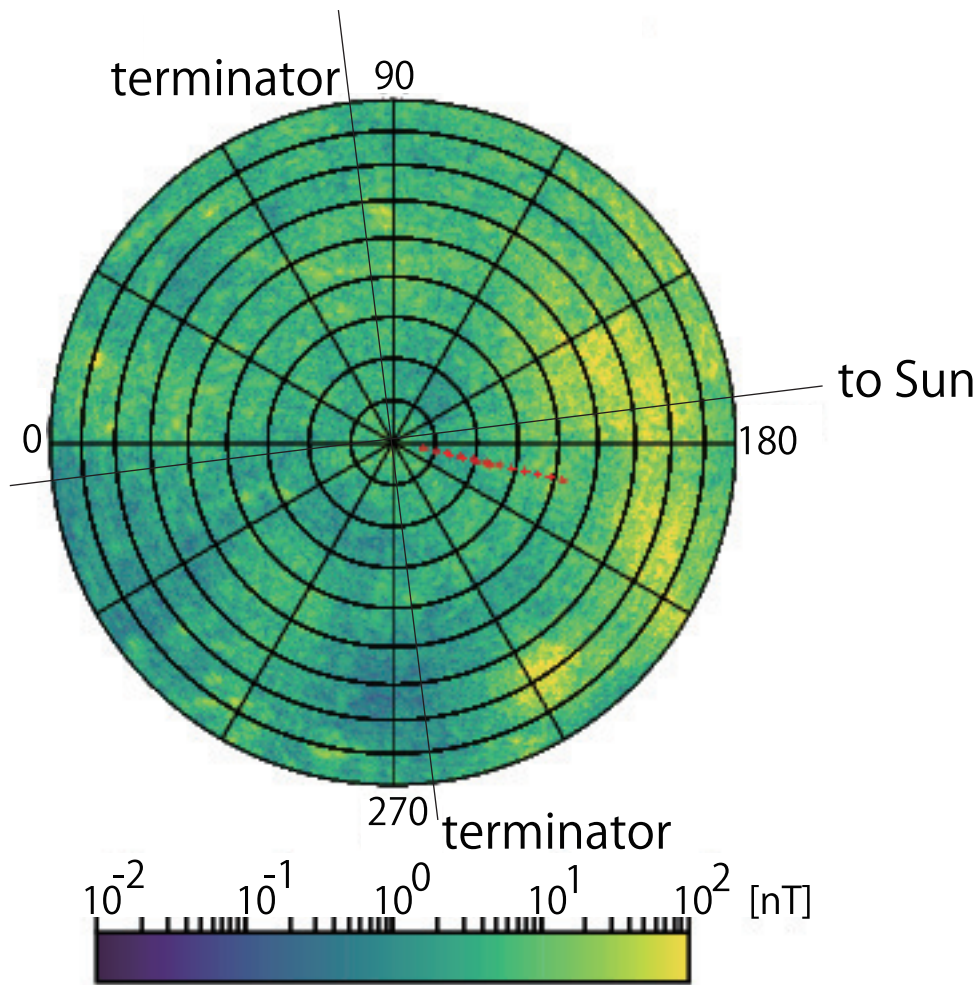
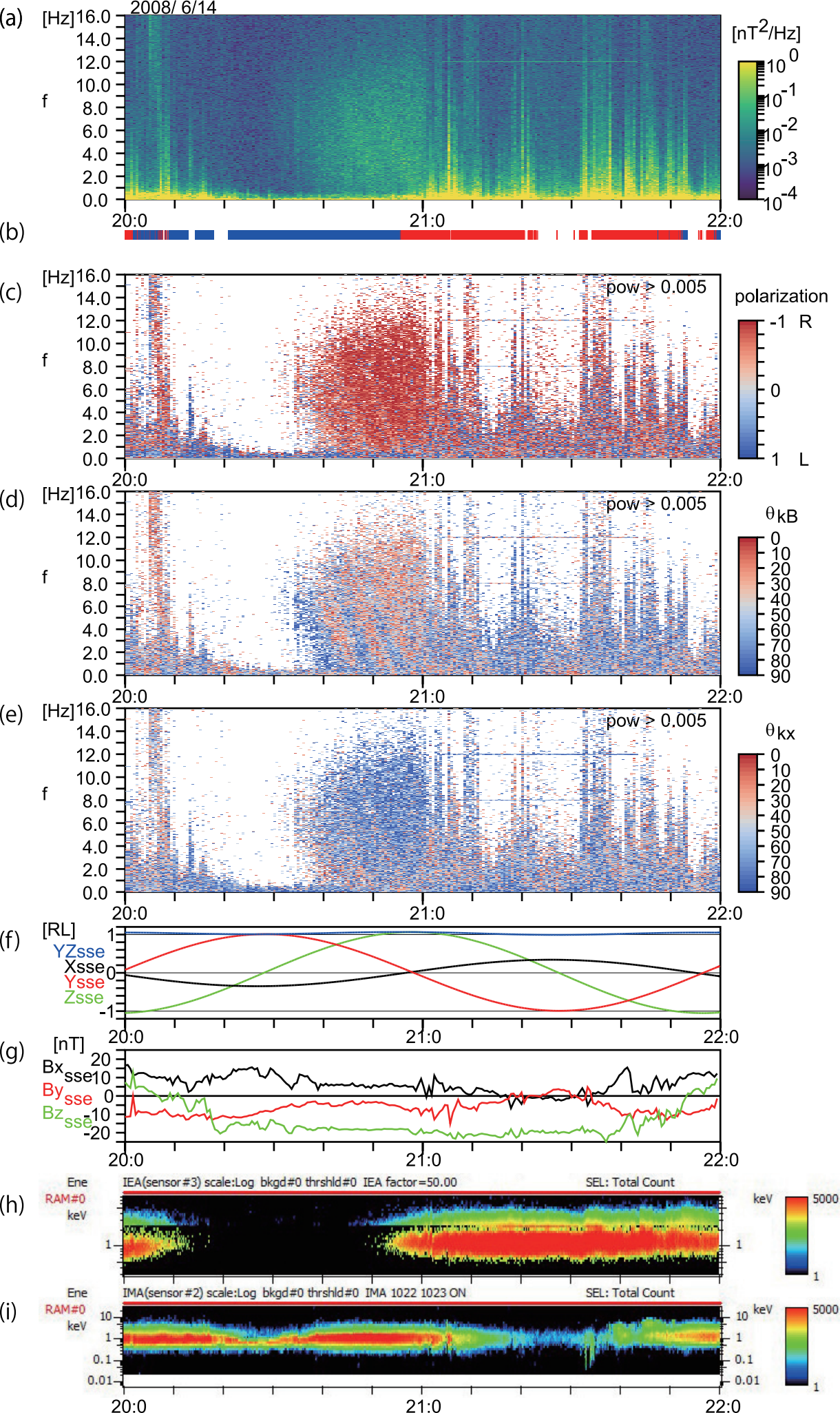


Figure 6.



**Figure 7.**

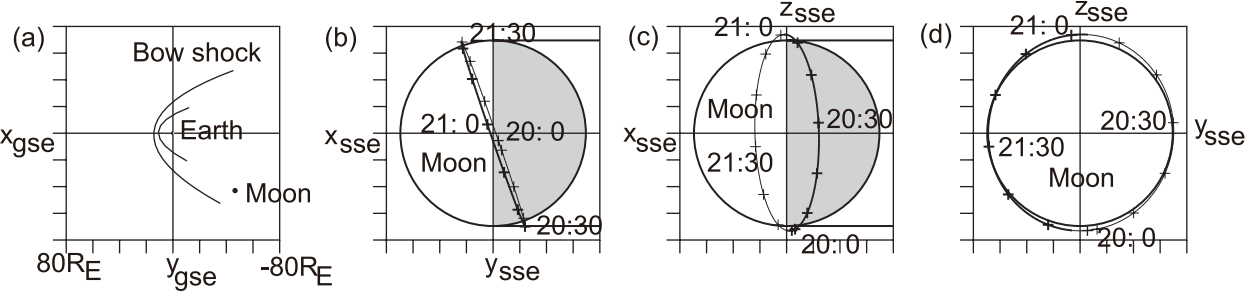


Figure 8.

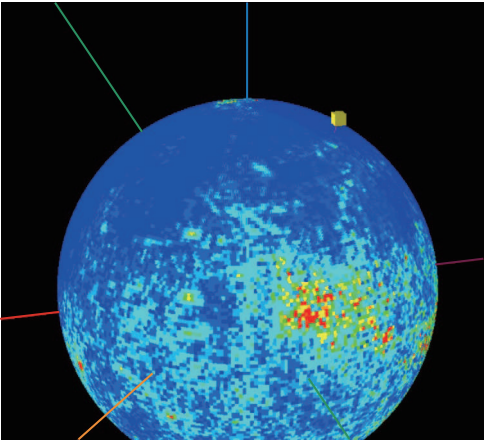


Figure 9.

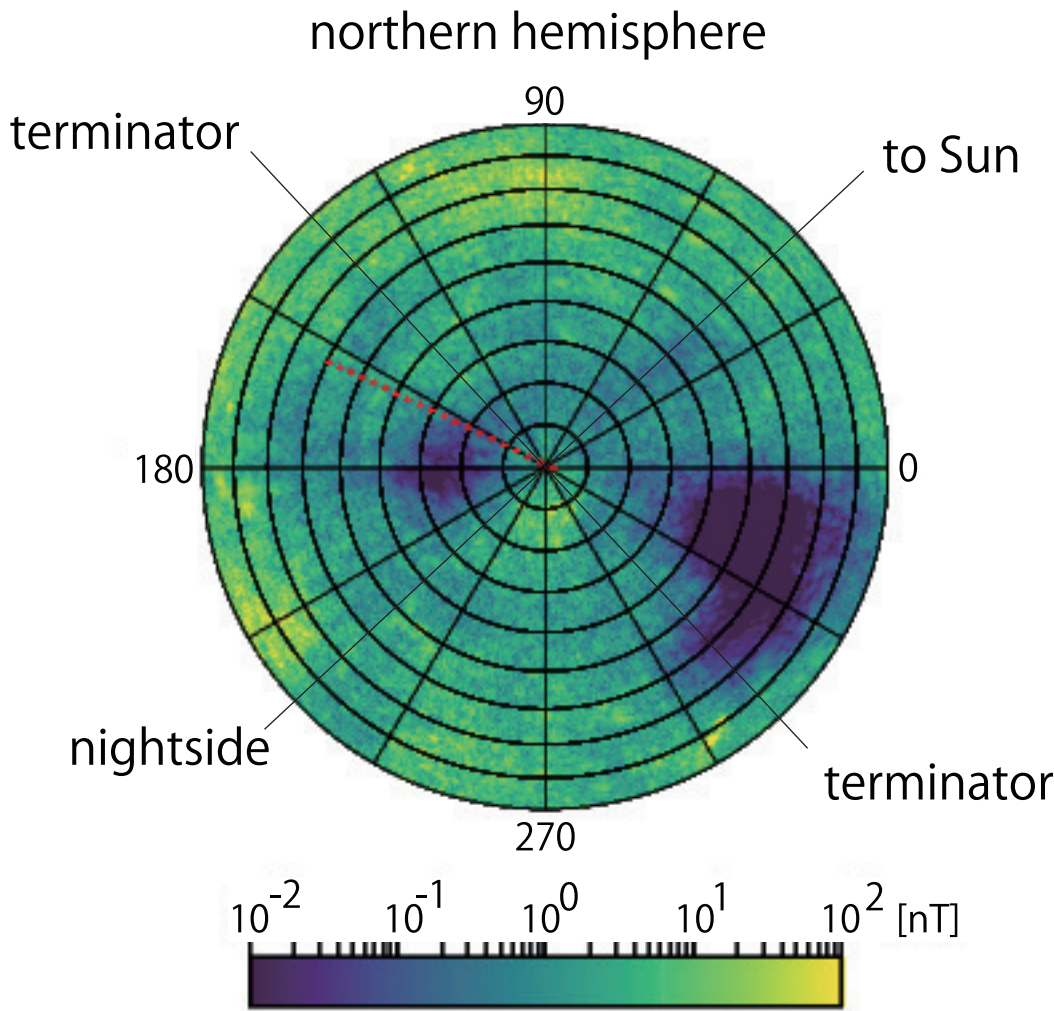
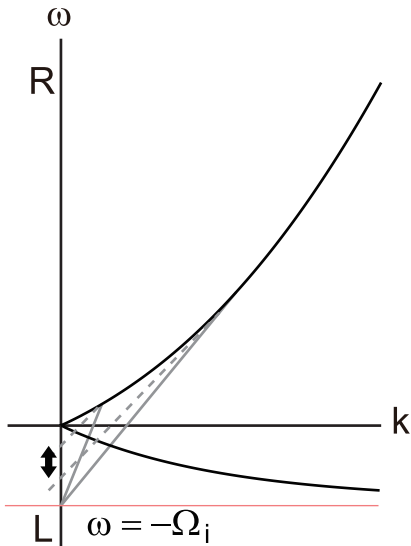


Figure 10.

(a)



(b)

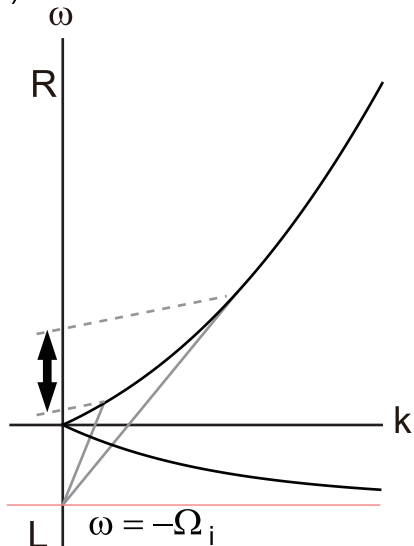


Figure 11.

Jun 14, 2008 20:58

$VA = 150$  km/s  $kV_{sw}/|k| = 100$  km/s

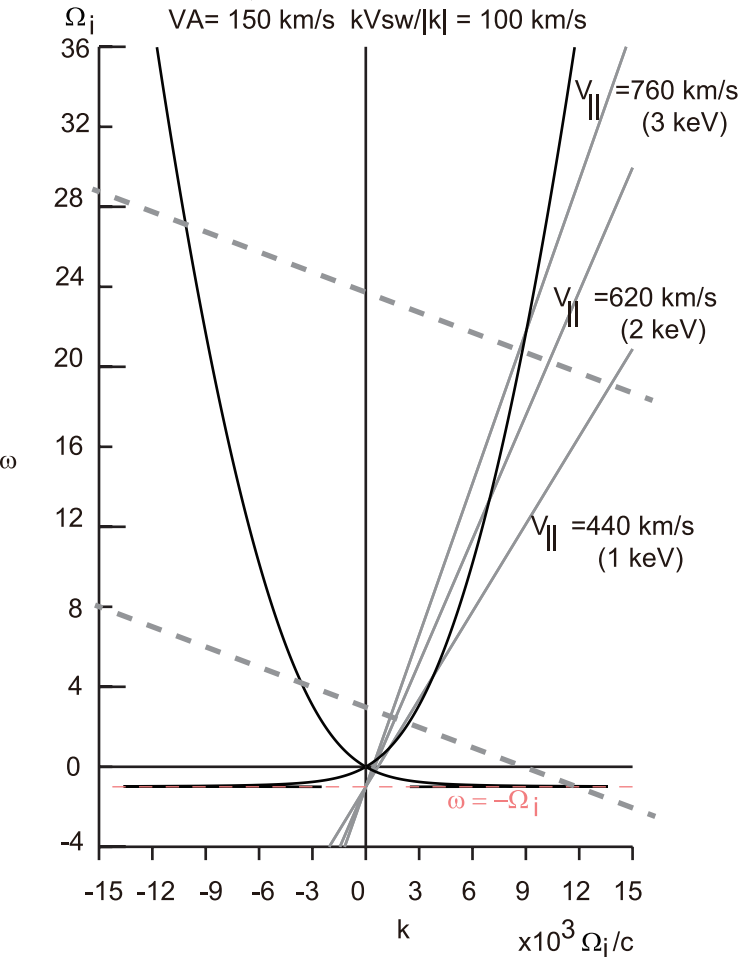


Figure 12.

Mar 8, 2008 7:05

$V_A = 38 \text{ km/s}$   $kV_{sw}/|k| = 24 \text{ km/s}$

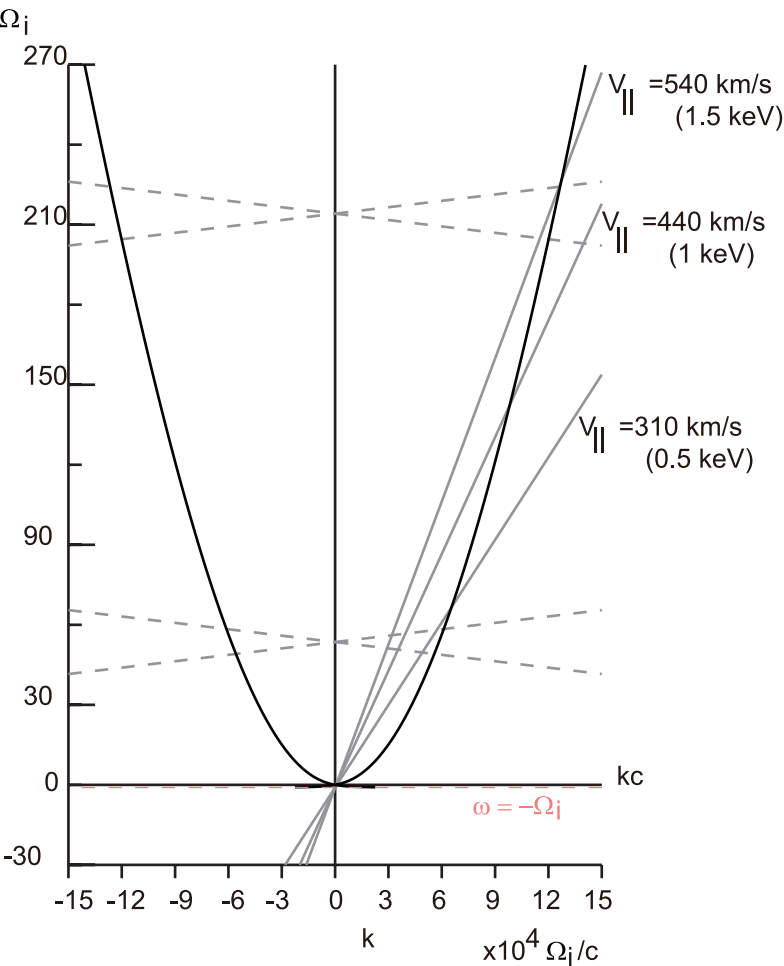


Figure 13.

